

Data-Efficient Generative Modeling of Non-Gaussian Global Climate Fields via Scalable Composite Transformations

Johannes Brachem^{*1}, Paul F.V. Wiemann², and Matthias Katzfuss³

¹Chair of Statistics, University of Göttingen, Germany

²Department of Statistics, The Ohio State University, USA

³Department of Statistics, University of Wisconsin–Madison, USA

Abstract

Quantifying uncertainty in future climate projections is hindered by the prohibitive computational cost of running physical climate models, which severely limits the availability of training data. We propose a data-efficient framework for emulating the internal variability of global climate fields, specifically designed to overcome these sample-size constraints. Inspired by copula modeling, our approach constructs a highly expressive joint distribution via a composite transformation to a multivariate standard normal space. We combine a nonparametric Bayesian transport map for spatial dependence modeling with flexible, spatially varying marginal models, essential for capturing non-Gaussian behavior and heavy-tailed extremes. These marginals are defined by a parametric model followed by a semi-parametric B-spline correction to capture complex distributional features. The marginal parameters are spatially smoothed using Gaussian-process priors with low-rank approximations, rendering the computational cost linear in the spatial dimension. When applied to global log-precipitation-rate fields at more than 50,000 grid locations, our stochastic surrogate achieves high fidelity, accurately quantifying the climate distribution’s spatial dependence and marginal characteristics, including the tails. Using only 10 training samples, it outperforms a state-of-the-art competitor trained on 80 samples, effectively octupling the computational budget for climate research. We provide a Python implementation at <https://github.com/jobrachem/ppptm>.

Keywords: Emulating internal climate variability, Gaussian processes, Stochastic surrogate, Non-Gaussian spatial field, Transformation model

*brachem@uni-goettingen.de

1. Introduction

While modern physical climate models are essential for understanding global climate patterns and their development under different conditions, assessing their uncertainty remains a challenge. It often involves ensembles of outcomes obtained by running the models repeatedly under randomly perturbed initial conditions to capture internal climate variability, a process with prohibitive computational demand that limits research. Emulating internal variability via statistical generative modeling of climate-model output alleviates these constraints by enabling the rapid generation of new random samples. However, this task is complicated by the high dimensionality and starkly non-Gaussian nature of the target spatial fields and, due to the cost of running the physical models, the limited availability of training data.

Formally, we estimate the distribution of a non-Gaussian spatial field $\mathbf{y} = (y_1, \dots, y_L)^\top$ from a collection of training samples $\mathbf{y}_1, \dots, \mathbf{y}_N$ produced by the climate model, where the dimension is potentially very high (e.g., $L > 50,000$) and the sample size is small (typically $10 \leq N \leq 100$). In this text, we demonstrate our method on $N \leq 98$ samples of global log precipitation rates (m/s) on a roughly 1° longitude-latitude grid of size $L = 288 \times 192 = 55,296$ from the Community Earth System Model (CESM) Large Ensemble Project (Kay et al., 2015); see bottom left panel of Figure 1.

We propose a statistical model that achieves high fidelity and that fits and generates hundreds of new samples in minutes on a standard laptop. (In contrast, a single run of the CESM model can take weeks on a supercomputer.) Our model is defined as an invertible composite map from the response space to a multivariate standard Gaussian space, as illustrated in Figure 1. The composition consists of an elementwise marginal model (combining a parametric distribution with a flexible semi-parametric transformation) and a triangular scalable Bayesian transport map (Katzfuss & Schäfer, 2023). The parametric model serves as a first effort to marginally Gaussianize the elements of \mathbf{y} by fitting a parametric distribution and mapping into the Gaussian space via the probability transformation. The semi-parametric transformation provides a regularized correction for residual misfit in the parametric model via a second marginal Gaussianization step. As we show below, this composite construction allows the parametric component to control the marginal tails, while the semi-parametric component captures deviations from this baseline in the bulk of the distribution. The triangular Bayesian transport map acts as a copula, describing dependence, an idea proposed for a special (linear) case of the Bayesian transport map by Li and Shand (2022). Our construction effectively handles even complex marginal distributions.

Our main contribution lies in the design of the composite model architecture in general and in the development of a well-behaved parameterization and scalable, spatially smoothed estimation of the semi-parametric transformation in particular. These innovations provide a targeted boost in flexibility that allows the model to make highly efficient use of the information provided by the data while controlling the risk of overfitting through regularization. As a result, our model surpasses the performance of previous state-of-the-art approaches even when trained on only a quarter of the sample size. While it is motivated by a spatial problem, and we make use of spatial language throughout the text, the model is in principle applicable to any \mathbf{y} admitting a meaningful notion of distance between its entries.

Related existing methods generally fall into three categories: those relying on restrictive assumptions, those that scale poorly to large dimensions L , or those requiring large numbers of training replicates N .

The first category includes models that implicitly or explicitly assume Gaussianity, like Gaussian-process (GP) models with parametric covariance functions (see, for example, Banerjee et al., 2014) or extensions of GP models to nonstationary or nonparametric covariances (Choi et al., 2013; Porcu et al., 2021; Risser, 2016). This category also includes methods specifically developed for climate-model emulation (Nychka et al., 2018; Wiens et al., 2020). Other GP

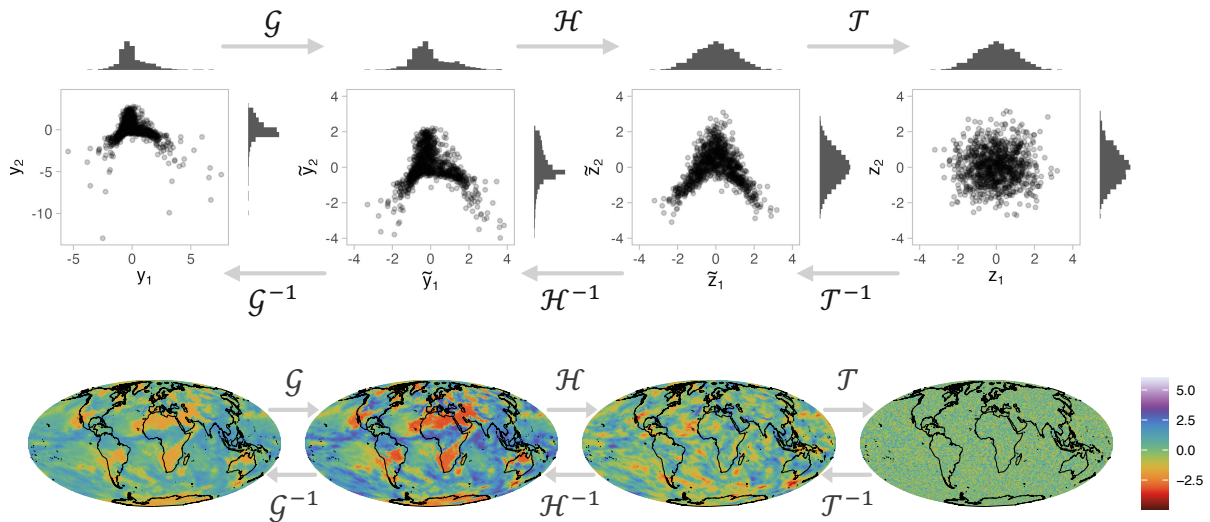


Figure 1 Top: Conceptual illustration of the three-part composite transformation mapping a bivariate non-Gaussian distribution to a standard Gaussian distribution. The parametric marginal model \mathcal{G} (here, a location-scale t -distribution), standardizes the margins and brings the tails closer to the bulk of the distribution. The semi-parametric model \mathcal{H} corrects residual deviations from marginal Gaussianity. Finally, the Bayesian transport map \mathcal{T} captures and removes the nonlinear dependence, achieving joint Gaussianity. Bottom: Analogous transformation of a global log-precipitation-rate field produced by a climate model (see main text). Due to the joint estimation of \mathcal{G} and \mathcal{H} here, the behavior of \mathcal{G} cannot be easily interpreted separately from \mathcal{H} .

approaches are tailored to non-Gaussian data but cover only a limited range of dependence structures, since they still rely on GP covariance functions (Gelfand & Schliep, 2016; Xu & Genton, 2017). Multivariate transformation models (Klein et al., 2022) are a non-GP model class that combines flexible marginal models with a Gaussian copula and provides inspiration for our semi-parametric marginal layer, but the Gaussian copula assumption scales poorly with dimension and again limits the type of dependence that can be captured.

The second category includes graphical transformation models (Herp et al., 2024), which focus on the discovery of conditional independence in a semiparametrically estimated non-Gaussian dependence structure with tens to hundreds of dimensions, and other copula models. While copulas can represent non-Gaussian dependence and have been tailored to spatial data (e.g. Krupskii et al., 2018; Mondal et al., 2024), current methods for high-dimensional copulas target only hundreds (Müller & Czado, 2019a) to roughly 2,100 dimensions (Müller & Czado, 2019b).

The third category includes deep learning methods like normalizing flows (Kobyzev et al., 2021), variational autoencoders (VAE), and generative adversarial networks (GANs). These methods have been applied to spatial problems in general (Ng & Zammit-Mangion, 2022, 2023), and to climate model emulation in particular (Ayala et al., 2021; Besombes et al., 2021). Unlike our data-efficient approach, these methods typically require thousands of training samples and struggle to capture complex dependencies when restricted to the small sample sizes ($N \approx 10 - 100$) typical of climate ensembles.

The remainder of this article is organized as follows. In Section 2, we provide a detailed description of our model, in Section 3 we describe our estimation procedure, in Section 4 we apply our model to climate model output data on a large global grid, and in Section 5 we conclude. A Python implementation of our model is available as a Python library hosted on GitHub (<https://github.com/jobrachim/ppptm>), building on the probabilistic programming framework Liesel (Riebl et al., 2023) and a Python implementation of the Bayesian transport map (<https://github.com/katzfuss-group/batram>).

2. Model

2.1. Overview

Consider a continuous random vector $\mathbf{y} = (y_1, \dots, y_L)^\top$, for example representing a spatial field at L locations or grid points. We model the joint distribution of \mathbf{y} using a three-part composition $(\mathcal{T} \circ \mathcal{H} \circ \mathcal{G})$ mapping to a multivariate standard Gaussian space:

$$(\mathcal{T} \circ \mathcal{H} \circ \mathcal{G})(\mathbf{y}) \sim \mathcal{N}_L(\mathbf{0}, \mathbf{I}), \quad (1)$$

where \mathcal{H} and \mathcal{G} are spatially smoothed element-wise operators ensuring that marginally $(\mathcal{H}_i \circ \mathcal{G}_i)(y_i) \sim \mathcal{N}(0, 1)$ for all $i = 1, \dots, L$. For \mathcal{G} , we construct a preliminary element-wise transformation based on a manually chosen parametric distributional family. For \mathcal{H} , we build on work on conditional transformation models (Hothorn et al., 2018) and penalized transformation models (Brachem et al., 2025) to construct a semi-parametric second layer of element-wise transformations. For \mathcal{T} , we employ the triangular scalable Bayesian transport map proposed by Katzfuss and Schäfer (2023). Details on all parts of the composition are provided in the following sections. We denote intermediate quantities as:

$$\tilde{\mathbf{y}} = \mathcal{G}(\mathbf{y}) \quad (2)$$

$$\tilde{\mathbf{z}} = \mathcal{H}(\tilde{\mathbf{y}}) = (\mathcal{H} \circ \mathcal{G})(\mathbf{y}) \quad (\text{marginally Gaussian}) \quad (3)$$

$$\mathbf{z} = \mathcal{T}(\tilde{\mathbf{z}}) = (\mathcal{T} \circ \mathcal{H} \circ \mathcal{G})(\mathbf{y}) \quad (\text{jointly Gaussian}). \quad (4)$$

Given the triangular structure of $\mathcal{T} = (\mathcal{T}(\tilde{z}_1), \mathcal{T}(\tilde{z}_{1:2}), \dots, \mathcal{T}_L(\tilde{z}_{1:L}))^\top$ and the element-wise nature of \mathcal{G} and \mathcal{H} , the joint density of \mathbf{y} factorizes as:

$$p(\mathbf{y}) = \prod_{i=1}^L \left(\phi(\mathcal{T}_i(\tilde{z}_{1:i})) \times \left| \frac{\partial \mathcal{T}_i(\tilde{z}_{1:i})}{\partial \tilde{z}_i} \right| \times \left| \frac{\partial \mathcal{H}_i(\tilde{y}_i)}{\partial \tilde{y}_i} \right| \times \left| \frac{\partial \mathcal{G}_i(y_i)}{\partial y_i} \right| \right), \quad (5)$$

where ϕ denotes the standard Gaussian probability density function (PDF). All three parts of the composition are invertible, so the model can be used to generate new samples by drawing $\mathbf{z}^* \sim \mathcal{N}(\mathbf{0}, \mathbf{I})$ and computing $\mathbf{y}^* = (\mathcal{G}^{-1} \circ \mathcal{H}^{-1} \circ \mathcal{T}^{-1})(\mathbf{z}^*)$. Closed-form inverses exist for \mathcal{G} and \mathcal{T} (see Subsection 2.3 and Subsection 3.2), while \mathcal{H}^{-1} is approximated numerically.

2.2. Copula-inspired separation of marginal and dependence models

Our approach is grounded in the separation of marginal and joint distributions established by Sklar's theorem (1959), the foundation of copula models. However, we (equivalently) map to a standard Gaussian space instead of the conventional standard uniform space. This choice simplifies the development of \mathcal{H} , offering direct control over marginal tail behavior, and it aligns with the scalable Bayesian transport map \mathcal{T} , which targets a standard Gaussian.

In our model, the marginal distributions are characterized by the composition of \mathcal{H} and \mathcal{G} . For any continuous univariate random variable y_i , there exists a unique strictly monotonically increasing transformation to the standard Gaussian space, $h_i = \Phi^{-1} \circ F_i$, such that $F_i(y_i) = \Phi(h_i(y_i))$ and $h_i(y_i) \sim \mathcal{N}(0, 1)$, where Φ is the standard Gaussian CDF and F_i is y_i 's CDF (see Corollary 1 in Hothorn et al., 2018). We model these transformations as $h_i = \mathcal{H}_i \circ \mathcal{G}_i$, where \mathcal{G}_i is a parametric base model (see Subsection 2.3) and \mathcal{H}_i is a semi-parametric B-spline correction (see Subsection 2.4). Jointly applying \mathcal{G}_i and \mathcal{H}_i results in a marginally Gaussianized vector $\tilde{\mathbf{z}} = (\mathcal{H} \circ \mathcal{G})(\mathbf{y})$.

The dependence structure of $\tilde{\mathbf{z}}$ is captured by a multivariate transformation to a multivariate standard Gaussian space, $\mathcal{T} : \mathbb{R}^L \rightarrow \mathbb{R}^L$, such that $\mathbb{P}(\tilde{\mathbf{z}} \leq \mathbf{t}) = \Phi_L(\mathcal{T}(\mathbf{t}))$ and $\mathcal{T}(\tilde{\mathbf{z}}) \sim \mathcal{N}(\mathbf{0}, \mathbf{I})$, where Φ_L denotes the L -dimensional standard Gaussian CDF. Without loss of generality, we

can assume this transformation \mathcal{T} to be lower triangular, where each $\mathcal{T}_i(\tilde{\mathbf{z}}_{1:i})$ is increasing in \tilde{z}_i (Rosenblatt, 1952). We adopt the parameterization $\mathcal{T}_i(\tilde{\mathbf{z}}_{1:i}) = (\tilde{z}_i - f_i(\tilde{\mathbf{z}}_{<i}))/d_i$ with $d_i \in \mathbb{R}^+$, $f_i : \mathbb{R}^{i-1} \rightarrow \mathbb{R}$ for $i = 2, \dots, L$, and $f_i(\tilde{\mathbf{z}}_{<i}) \equiv 0$ for $i = 1$. The triangular map \mathcal{T} takes the role of a copula, describing the dependence structure of the marginally transformed data $\tilde{\mathbf{z}}$. \mathcal{T} can also be understood as a series of nonlinear regressions $\tilde{z}_i = f_i(\tilde{\mathbf{z}}_{<i}) + \epsilon_i$, with $\epsilon_i \sim \mathcal{N}(0, d_i^2)$. Crucially, the triangular structure implies that the first element of $\tilde{\mathbf{z}}$ is modeled as Gaussian, and subsequent elements as conditionally Gaussian. For variables appearing early in the ordering sequence, the conditioning set provides limited predictive information, effectively reducing the conditional Gaussian assumption to an unconditional one. This necessitates the accurate marginal Gaussianization provided by \mathcal{G} and \mathcal{H} , as the transport map cannot correct marginal deviations especially for these early-ordered variables.

2.3. Details on the parametric transformations \mathcal{G}

The parametric transformations \mathcal{G}_i are defined as $\tilde{y}_i = \mathcal{G}_i(y_i) = \Phi^{-1}(F_i(y_i|\boldsymbol{\zeta}_i))$, where F_i is a user-specified parametric CDF governed by unknown parameters $\boldsymbol{\zeta}_i$, and Φ^{-1} is the standard Gaussian quantile function. We assume that F_i admits a density. This parametric transformation is strictly monotonically increasing by construction. By the chain rule, the derivative is $\frac{\partial}{\partial y_i} \mathcal{G}_i(y_i) = F'_i(y_i|\boldsymbol{\zeta}_i)\phi(\mathcal{G}_i(y_i))^{-1}$, where ϕ is the standard Gaussian density and F'_i is the density corresponding to F_i . The inverse parametric transformation is $y_i = \mathcal{G}_i^{-1}(\tilde{y}_i) = F_i^{-1}(\Phi(\tilde{y}_i)|\boldsymbol{\zeta}_i)$. As a concrete example, if F_i is Gaussian with mean μ_i and variance σ_i^2 , then $\mathcal{G}_i(y_i) = (y_i - \mu_i)/\sigma_i$ simplifies to a location-scale transformation. For simplicity, we assume the same distributional family F is chosen for all locations $i = 1, \dots, L$.

When the number of training replicates N is small, estimating $\boldsymbol{\zeta}_i$ independently at each spatial location is difficult. However, because geophysical processes typically vary smoothly, it is reasonable to assume spatial smoothness for the distributional parameters. To regularize estimation and share information across space, we place Gaussian-process (GP) priors over space on the parameters $\boldsymbol{\zeta}_i$. Specifically, let $\boldsymbol{\zeta}_i = [\zeta_{i,1}, \dots, \zeta_{i,P}]$, where P denotes the number of parameters modeled in the parametric marginal distribution F_i . We define independent GP priors $\zeta_{i,p} \sim \mathcal{GP}(0, k_{\zeta_p}(\cdot, \cdot))$, for each $p = 1, \dots, P$, where k_{ζ_p} denotes an appropriate correlation function. Each process and associated kernel k_{ζ_p} is governed by hyperparameters $\boldsymbol{\theta}_p^{\mathcal{G}}$, typically comprising an amplitude $\tau_p^{\mathcal{G}}$ and a length scale $\ell_p^{\mathcal{G}}$, such that $\boldsymbol{\theta}_p^{\mathcal{G}} = (\tau_p^{\mathcal{G}}, \ell_p^{\mathcal{G}})^{\top}$.

2.4. Details on the semi-parametric transformations \mathcal{H}

We design the semi-parametric transformations \mathcal{H}_i to provide flexible corrections to the parametric base model \mathcal{G} within the bulk of the data distribution, while seamlessly reverting to the parametric tails for robust extrapolation.

We parameterize $\mathcal{H}_i : \mathbb{R} \rightarrow \mathbb{R}$ as a strictly monotonically increasing B-spline on the interval $[k_1, k_m]$, given by

$$\mathcal{H}_i(\tilde{y}_i) = \sum_{j=1}^J B_j(\tilde{y}_i) \left(\gamma_{1,i} + \sum_{\ell=2}^j \exp(\gamma_{\ell,i}) \right), \quad \text{if } \tilde{y}_i \in [k_1, k_m], \quad (6)$$

and the identity function if $\tilde{y}_i \in (-\infty, k_1) \cup (k_m, \infty)$. The functions B_j are cubic B-spline bases defined on a sequence of $J + 4$ knots $k_{-2} < k_{-1} < \dots < k_{m+3}$, where k_1, \dots, k_m are the *interior knots* with $m = J - 2$. The knots are constant across all dimensions $i = 1, \dots, L$. The knot sequence is defined as an equidistant grid with $k_{j+1} - k_j = k$ denoting the constant difference between two adjacent knots, and they are set up by choosing $k_2 = a$ and $k_{m-1} = b$ using Theorem 2 (see below). The vector $\boldsymbol{\gamma}_i \in \mathcal{K} \subset \mathbb{R}^J$ contains an intercept parameter $\gamma_{1,i}$ and log-increments in the spline parameters, $\gamma_{2,i}, \dots, \gamma_{J,i}$, ensuring monotonicity. To enforce the identity behavior outside $[a, b]$ and ensure C^2 continuity at the boundaries, we impose

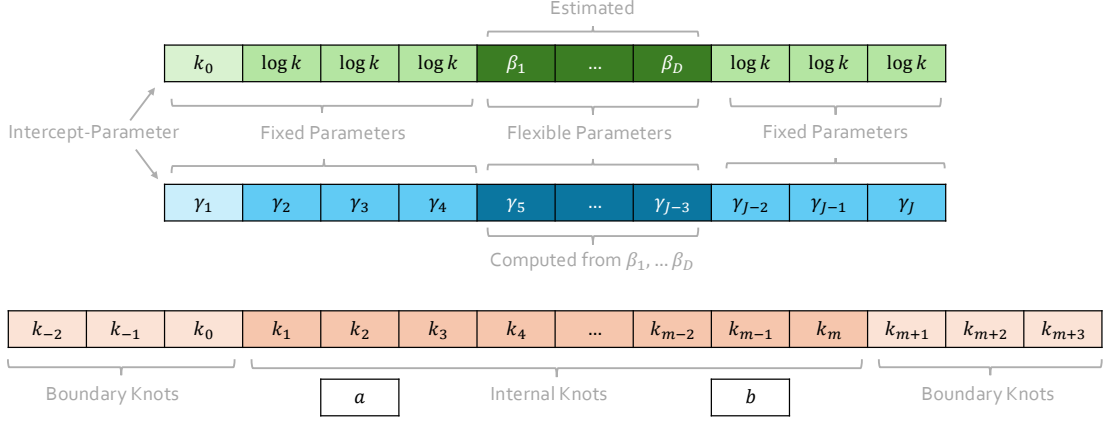


Figure 2 Illustration of how parameters and knots in our modified monotonically increasing B-spline relate to each other. The bottom panel (orange) shows the knots. The middle panel (blue) shows the spline parameters on the level of $\gamma_1, \dots, \gamma_J$, aligned with corresponding knots. The top panel (green) shows the values of the fixed γ parameters, and aligns the freely estimated parameters β_1, \dots, β_D with their counterparts $\gamma_5, \dots, \gamma_{J-3}$ (see (7)). Note that $k = k_{j+1} - k_j$ is the (constant) distance between two adjacent knots, and that $J = D + 7$ and $m = D + 5$.

specific constraints on the coefficients. To match the slope and level of the identity function, we fix the first coefficient to $\gamma_{1,i} = k_0$ for all locations i , and we fix three $\gamma_{j,i} = \log(k)$ for $j \in \{2, 3, 4\} \cup \{J - 2, J - 1, J\}$ on either side of the knot basis. The remaining log-increments are parameterized via unconstrained parameters $\beta_i \in \mathbb{R}^D$ ($D = J - 7$):

$$\gamma_{j,i} = \beta_{j-4,i} - \log \left(\frac{\sum_{d=1}^D \exp(\beta_{d,i})}{(m-5)k} \right), \quad \text{for } j = 5, \dots, J-3. \quad (7)$$

This normalization ensures that the spline traverses the vertical distance between the fixed endpoints exactly, preserving the identity mapping constraints. To emphasize the dependence on the unconstrained parameters β_i , we write $\mathcal{H}_i(\cdot | \beta_i)$ in the following. Figure 2 provides an overview of the parameters and knots in our modified monotonically increasing spline. Panel a) in Figure 3 illustrates the construction of \mathcal{H}_i using randomly sampled β_i . We now establish key theoretical properties that justify this architecture. Proofs are given in Appendix A.

Theorem 1 (Reduction to base model). *Let $(\mathcal{H}_i \circ \mathcal{G}_i)(y_i) \sim \mathcal{N}(0, 1)$, with \mathcal{H}_i as defined above and $\mathcal{G}_i(y_i) = \Phi^{-1}(F_i(y_i))$, where $F_i : \mathbb{R} \rightarrow [0, 1]$ is a continuous cumulative distribution function. If $\beta_i = \beta_i \mathbf{1}_D$ for any constant $\beta_i \in \mathbb{R}$, then $\mathbb{P}(y_i \leq t) = F_i(t)$ for all $t \in \mathbb{R}$.*

This theorem provides a clear mechanism for model parsimony: we can encourage the model to revert to the simpler parametric family F_i by shrinking the entries of β_i towards a constant value. This mechanism is the basis for our local regularization prior introduced below in Subsection 2.5.

Theorem 2 (Tail probabilities). *Let $(\mathcal{H}_i \circ \mathcal{G}_i)(y_i) \sim \mathcal{N}(0, 1)$, with \mathcal{H}_i as defined above and $\mathcal{G}_i(y_i) = \Phi^{-1}(F_i(y_i))$, where $F_i : \mathbb{R} \rightarrow [0, 1]$ is a continuous cumulative distribution function and Φ^{-1} is the standard normal quantile function. Further, let $q_a = F_i^{-1}(\Phi(a))$ and $q_b = F_i^{-1}(\Phi(b))$ be the quantiles of the distribution with CDF F_i at probability levels $\Phi(a)$ and $\Phi(b)$, respectively. Then $\mathbb{P}(y_i \leq t) = F_i(t)$ for all $t \in (-\infty, q_a] \cup [q_b, \infty)$.*

Consequently, tail behavior is determined entirely by the parametric choice F_i , decoupling the estimation of the bulk (where data are abundant) from the estimation of the tails (where data are scarce by definition). This is a major conceptual improvement over the transformation

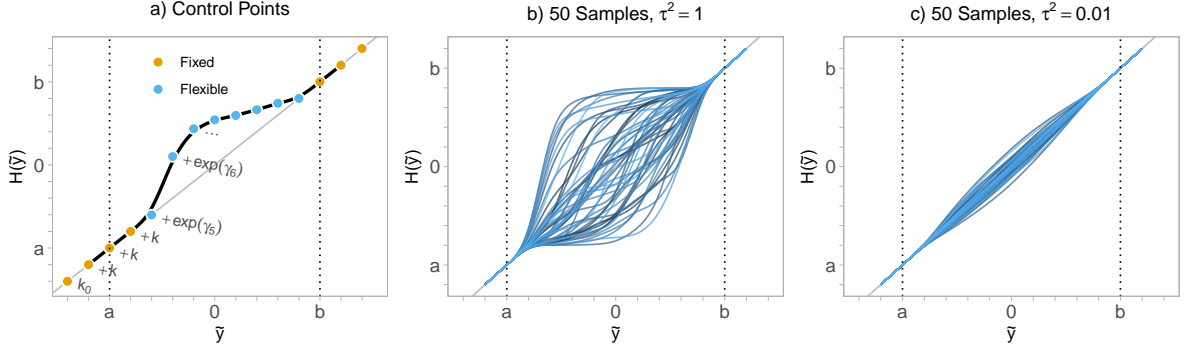


Figure 3 Panel a) illustrates our modified spline using a single random sample of β_i , which is transformed into γ using (7). The points are the B-spline control points $\gamma_{1,i} + \sum_{\ell=2}^j \exp(\gamma_{\ell,i})$, aligned with the knots k_0, \dots, k_{m+1} . Panels b) and c) each show 50 prior predictive samples of \mathcal{H}_i obtained by drawing β_i from our *onion prior* with variance parameters $\tau^2 = 1$ (b) and $\tau^2 = 0.01$ (c).

function used by Brachem et al. (2025), where the transformation function’s extrapolation behavior affects the implied tail densities. We set the boundaries at $-a = b = 4$ by default, implying that roughly 99.99% of the probability mass is modeled flexibly, while the extreme 0.01% relies on the robust parametric extrapolation. Other choices for a and b are possible if required by the application and if enough data is available.

2.5. Regularization for the semi-parametric transformations

Below, while we use the Bayesian terminology of “prior distributions” to motivate and construct regularization terms in \mathcal{H} and induce spatial information pooling in both \mathcal{H} and \mathcal{G} , note that these priors are employed merely as penalty functions, and parameter estimation is carried out by maximizing the unnormalized log posterior, resulting in maximum a posteriori (MAP) point estimates (see Section 3).

We design a prior for β_i with three goals in mind. First, the prior should regularize estimates of \mathcal{H}_i towards smoothness to combat overfitting. Second, it should penalize deviations of the marginal distributions from the base model by regularizing \mathcal{H}_i towards the identity function. Third, the prior should allow us to borrow information across space to improve estimation in the face of small numbers of training replicates.

The onion prior for local regularization. By Theorem 1, the marginal model for y_i collapses to the parametric base model F_i , if all elements of β_i are equal. We can thus regularize the marginal models towards the base models by penalizing differences in β_i . We achieve this penalization by placing a first-order random-walk prior on the elements of β_i , such that $\beta_{i,1} \sim \mathcal{N}(\beta, \tau^2)$ with starting condition β , and $\beta_{i,d} \sim \mathcal{N}(\beta_{i,d-1}, \tau^2)$ for subsequent $d = 2, \dots, D$. (We omit a subscript i on τ here, as we did not observe improved accuracy using location-specific τ values in our climate application.) The starting condition β is arbitrary, since it cancels out in (7); we therefore use $\beta = 0$ for simplicity. The resulting joint prior for β_i is given by $\beta_i \sim \mathcal{N}(\mathbf{0}, \tau^2 \mathbf{S})$, where \mathbf{S} is the (discrete) Brownian motion covariance matrix with entries $\mathbf{S}_{[r,c]} = \min(r, c)$. As $\tau^2 \rightarrow 0$, the elements of β_i are forced towards equality, such that by Theorem 1, the marginal model falls back to the base model F_i . In general, the elements of β_i are regularized towards similarity. This allows us to use a relatively generous default number of parameters (e.g., $D = 40$) to capture complex shapes when evident in the data, while automatically reverting to the smooth parametric form elsewhere. Panels b) and c) of Figure 3 show prior predictive samples of \mathcal{H}_i based on 50 random draws of β_i from this prior for $\tau^2 = 1$ (Panel b) and $\tau^2 = 0.01$ (Panel c). We find the pattern in Panel b) to be reminiscent of an onion cut in half, hence the name *onion prior*. This prior setup is closely related to penalized

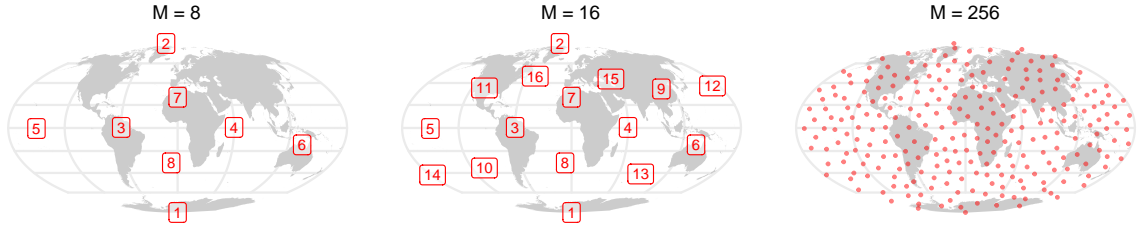


Figure 4 Illustration of the maximin ordering of locations on a global grid, showing the first M locations in red. In the left and middle panels, numbers indicate the position in the ordering. The maximin criterion places each new point to maximize the chordal distance to all preceding points, ensuring uniform global coverage. Apparent asymmetries in the early points arise from projecting this spherical optimization onto a 2D plane for plotting.

splines (see Lang & Brezger, 2004) and their adaptation in shape-constrained additive models (Pya & Wood, 2015).

Spatial smoothing. We extend the random-walk prior to incorporate spatial dependence using a multi-output GP construction (van der Wilk et al., 2020). Consider the Cholesky decomposition $\mathbf{S} = \mathbf{W}\mathbf{W}^\top$ of the Brownian motion covariance of β_i . We write $\beta_i = \mathbf{W}\tilde{\beta}_i \in \mathbb{R}^D$ for $i = 1, \dots, L$. For each $d = 1, \dots, D$, we define a latent spatial process $\tilde{\beta}_d \sim \mathcal{GP}(0, k_\beta(\cdot, \cdot))$ with shared amplitude τ and length scale $\ell^{\mathcal{H}}$. The latent coefficient vector $\tilde{\beta}_i$ is obtained by evaluating these processes at the location indexed by i . For L spatial locations, the resulting joint prior for $\beta = \text{vec}((\beta_1, \dots, \beta_L)^\top)$ collected at all locations has a separable covariance,

$$\beta \sim \mathcal{N}(\mathbf{0}_{LD}, \mathbf{K}_{\beta\beta}), \quad \mathbf{K}_{\beta\beta} = \mathbf{S} \otimes \tilde{\mathbf{K}}_{\beta\beta},$$

where the $L \times L$ spatial covariance matrix $\tilde{\mathbf{K}}_{\beta\beta}$ is obtained by evaluating $k_\beta(\cdot, \cdot)$ at the L locations.

2.6. Maximin ordering of \mathbf{y}

As in Katzfuss and Schäfer (2023), we use a maximum-minimum-distance (maximin) ordering (e.g., Guinness, 2018) of the elements of \mathbf{y} based on their locations. The ordering is meaningful for the triangular map \mathcal{T} and provides an effective method for selecting inducing locations for the low-rank approximations of the marginal models, described below in Section 3. Maximin ordering is achieved as follows. The first location is chosen arbitrarily. Subsequent locations are chosen sequentially such that the distance between each new location and its nearest neighbor among the previously chosen locations is as big as possible. Formally, let $\mathbf{s}_1, \dots, \mathbf{s}_L$ denote the unordered locations and $\mathbf{s}_{i_1}, \dots, \mathbf{s}_{i_L}$ the ordered locations, meaning that the ordering is encoded in the indices i_1, \dots, i_L . Arbitrarily start by setting $i_1 = 1$, then for $j = 2, \dots, L$ choose the next index as $i_j = \arg \max_{i \notin \mathcal{I}_{<j}} \min_{k \in \mathcal{I}_{<j}} \|\mathbf{s}_i - \mathbf{s}_k\|$, where $\mathcal{I}_{<j} = \{i_1, \dots, i_{j-1}\}$ holds the indices identifying the locations yet to be ordered. The resulting ordering of \mathbf{y} reflects a coarse spatial grid early in the ordering that transitions to finer grids later in the ordering. An illustration for a global grid is given in Figure 4.

2.7. Review of the scalable Bayesian transport map \mathcal{T}

We adopt the scalable Bayesian transport map of Katzfuss and Schäfer (2023), which decomposes the complex joint dependence into a sequence of univariate conditional regressions. The components of the triangular transport map \mathcal{T} are modeled as $\mathcal{T}_i(\tilde{\mathbf{z}}_{1:i}) = (\tilde{z}_i - f_i(\tilde{\mathbf{z}}_{<i}))d_i^{-1} \sim \mathcal{N}(0, 1)$. Gaussian-process inverse-Gamma priors are placed on the pairs (f_i, d_i) , with $d_i^2 \sim$

$\mathcal{IG}(\alpha_i, \beta_i)$ and $f_i|d_i \sim \mathcal{GP}(0, d_i^2 K_i)$. The key feature of the setup is the use of structure in $\tilde{\mathbf{z}}$ to drastically reduce the number of parameters that need to be estimated. Like Katzfuss and Schäfer (2023), we consider spatial information associated with each element \tilde{z}_i of $\tilde{\mathbf{z}}$ in the form of locations $\mathbf{s}_i \in \mathcal{S}$, $i = 1, \dots, L$, where \mathcal{S} is the spatial domain. Now, let $\delta_i = \min_{j \in 1, \dots, i-1} \|\mathbf{s}_i - \mathbf{s}_j\|$ denote the minimum distance between the location \mathbf{s}_i and any location $\mathbf{s}_1, \dots, \mathbf{s}_{i-1}$ that precedes \mathbf{s}_i in the ordering of $\tilde{\mathbf{z}}$.

Intuitively, a small δ_i means that, among the observations used to predict \tilde{z}_i , there is at least one observation from a nearby location. Thus, the smaller δ_i , the more representative $f_i(\tilde{\mathbf{z}}_{<i})$ is likely to be for \tilde{z}_i , and the smaller the conditional variance d_i^2 should be. Katzfuss and Schäfer (2023) apply results from Schäfer et al. (2021) to observe that a roughly power-functional decay of d_i^2 with respect to δ_i is plausible for the considered scenario. Reflecting this pattern, the prior for d_i^2 is set up with $\mathbb{E}(d_i^2) = \beta_i/(\alpha_i - 1) = \exp(\theta_1^d + \exp(\theta_2^d) \ln(\delta_i))$ and $\text{SD}(d_i^2) = g\mathbb{E}(d_i^2)$, which results in $\alpha_i = 2 + 1/g^2$ and $\beta_i = \exp(\theta_1^d + \theta_2^d \ln(\delta_i))(1 + 1/g^2)$. The hyperparameter θ_1^d is the logarithm of the expected variance if $\delta_i = 1$, while θ_2^d controls how the expected variance scales with increasing distance δ_i . The setup ensures that $\mathbb{E}(d_i^2)$ is increasing in δ_i . The constant $g \in \mathbb{R}_{>0}$ scales the prior standard deviation of d_i^2 relative to its expectation, where the default $g = 4$ is used to obtain a relatively weak prior.

The covariance function K_i in the Gaussian-process prior for f_i is designed to shrink f_i towards linearity with decreasing δ_i and let the contribution of each input $\tilde{z}_1, \dots, \tilde{z}_{i-1}$ decay exponentially according to its position when ordered by increasing distance to the location of \tilde{z}_i . These goals are achieved by letting

$$K_i(\tilde{\mathbf{z}}_{o(i)}, \tilde{\mathbf{z}}'_{o(i)}) = \mathbb{E}(d_i^2)^{-1} \left[\tilde{\mathbf{z}}_{o(i)}^\top \mathbf{Q}_i \tilde{\mathbf{z}}'_{o(i)} + \sigma_i^2 \rho \left(\gamma^{-1} \sqrt{(\tilde{\mathbf{z}}_{o(i)} - \tilde{\mathbf{z}}'_{o(i)})^\top \mathbf{Q}_i (\tilde{\mathbf{z}}_{o(i)} - \tilde{\mathbf{z}}'_{o(i)})} \right) \right], \quad (8)$$

which requires some elaboration. First, $\tilde{\mathbf{z}}_{o(i)}$ denotes a view of $\tilde{\mathbf{z}}_{<i}$ that is ordered in increasing distance to the location of \tilde{z}_i , such that $\tilde{z}_{o(i)_1}$ is the element of $\tilde{\mathbf{z}}_{<i}$ that is closest to \tilde{z}_i . Second, \mathbf{Q}_i is a diagonal matrix with the j^{th} diagonal element given by $\exp(-j \exp(\theta^q))$ for $j = 1, \dots, i-1$. This way, \mathbf{Q}_i both controls the linear part of f_i and encodes the decreasing contributions of inputs to f_i according to their distance to the location of \tilde{z}_i . Due to the ordering, larger j imply higher distance to the location of \tilde{z}_i , and thus the diagonal entries of \mathbf{Q}_i are decreasing in j . The hyperparameter θ^q controls how quickly they approach zero; with larger θ^q implying a steeper decrease. Third, ρ denotes a covariance function, where $\gamma = \exp(\theta^\gamma)$ serves as a range parameter, such that θ^γ is the log range. We use the Matérn covariance function with smoothness $3/2$. Fourth, $\sigma_i^2 = \exp(\theta_1^\sigma + \exp(\theta_2^\sigma) \ln(\delta_i))$ determines the extent of nonlinearity in f_i and decays similar to d_i^2 , rendering f_i to resemble a linear function more closely as δ_i decreases. The meaning of the hyperparameters θ_1^σ and θ_2^σ is analogous to θ_1^d and θ_2^d , respectively. In sum, the scalable Bayesian transport map is governed by the six hyperparameters $\boldsymbol{\theta}^\mathcal{T} = (\theta_1^d, \theta_2^d, \theta^q, \theta^\gamma, \theta_1^\sigma, \theta_2^\sigma)^\top \in \mathbb{R}^6$. For given \tilde{z}_i and $\boldsymbol{\theta}^\mathcal{T}$, the Gaussian-process inverse-gamma priors on (f_i, d_i^2) is conjugate, such that a posterior transport map is available in closed form.

3. Parameter estimation and computational complexity

The model involves three sets of unknown parameters: the parametric marginal parameters $\boldsymbol{\zeta}$ and hyperparameters $\boldsymbol{\theta}^\mathcal{G}$ in \mathcal{G} , where $\boldsymbol{\zeta} = \text{vec}((\boldsymbol{\zeta}_1, \dots, \boldsymbol{\zeta}_L)^\top)$, the semi-parametric marginal parameters $\boldsymbol{\beta}$ and hyperparameters $\boldsymbol{\theta}^\mathcal{H}$ in \mathcal{H} , where $\boldsymbol{\beta} = \text{vec}((\boldsymbol{\beta}_1, \dots, \boldsymbol{\beta}_L)^\top)$, and the transport-map hyperparameters $\boldsymbol{\theta}^\mathcal{T}$ in \mathcal{T} . Joint estimation of all parameters is computationally intractable due to the combination of the non-Gaussian semi-parametric likelihood and the massive dimensionality. Therefore, we adopt a two-stage estimation strategy, common in copula literature (Joe, 2005): we first estimate the marginal models (parametric + semi-parametric) jointly under a working assumption of spatial independence of $\tilde{\mathbf{z}}$, and then estimate the spatial dependence in $\tilde{\mathbf{z}}$ (transport map) given the fitted marginals.

3.1. Stage 1: Scalable marginal-model estimation

Low-rank approximation. Direct evaluation of the priors for ζ and β scales as $\mathcal{O}(PL^3)$ and $\mathcal{O}(L^3)$, respectively, due to the necessity to invert the $L \times L$ spatial covariance matrices $\mathbf{K}_{\zeta_p \zeta_p}$ and $\tilde{\mathbf{K}}_{\beta\beta}$. We overcome this bottleneck using a low-rank approximation based on $M \ll L$ inducing locations, selected as the first M points in a maximum-minimum-distance ordering (see [Subsection 2.6](#) and [Figure 4](#)), which we describe for β and apply analogously to ζ . We parameterize the multivariate spatial field $\beta \in \mathbb{R}^{LD}$ through whitened inducing variables $\mathbf{u} \sim \mathcal{N}(\mathbf{0}_{MD}, \mathbf{I}_{MD})$ at these M locations, writing

$$\beta = \mathbf{B}(\boldsymbol{\theta}^{\mathcal{H}})\mathbf{u}, \quad \text{where} \quad \mathbf{B}(\boldsymbol{\theta}^{\mathcal{H}}) = \mathbf{K}_{\beta\mathbf{u}}\mathbf{K}_{\mathbf{u}\mathbf{u}}^{-1}\mathbf{L}, \quad (9)$$

with $\mathbf{K}_{\mathbf{u}\mathbf{u}} = (\mathbf{S} \otimes \tilde{\mathbf{K}}_{\mathbf{u}\mathbf{u}})$ and $\mathbf{L}\mathbf{L}^{\top} = \mathbf{K}_{\mathbf{u}\mathbf{u}}$, such that \mathbf{L} is the lower Cholesky factor of the covariance matrix at the locations of the inducing variables, $\mathbf{L}\mathbf{u} \sim \mathcal{N}(\mathbf{0}_M, \mathbf{K}_{\mathbf{u}\mathbf{u}})$. This approach corresponds to projected process prediction in Rasmussen and Williams (2008), with implied prior covariance $\mathbf{K}_{\beta\beta} = \mathbf{K}_{\beta\mathbf{u}}\mathbf{K}_{\mathbf{u}\mathbf{u}}^{-1}\mathbf{K}_{\mathbf{u}\beta}$, and can be interpreted as a basis-function parameterization with the covariance function acting as a (hyperparameter-dependent) basis function and \mathbf{u} acting as the coefficient vector. Instantiation of the full $(DL \times DM)$ matrix $\mathbf{K}_{\beta\mathbf{u}}$ can be avoided by exploiting its Kronecker structure to rewrite the model as $\beta = \text{vec}(\tilde{\mathbf{K}}_{\beta b} \tilde{\mathbf{L}}^{-\top} \mathbf{U} \mathbf{W}^{\top})$, where $\tilde{\mathbf{L}}\tilde{\mathbf{L}}^{\top} = \tilde{\mathbf{K}}_{\mathbf{u}\mathbf{u}}$, $\mathbf{W}\mathbf{W}^{\top} = \mathbf{S}$, \mathbf{U} is $M \times D$ so that $\mathbf{u} = \text{vec}(\mathbf{U})$, and $\tilde{\mathbf{K}}_{\beta b}$ of dimension $(L \times M)$ is the largest matrix. This low-rank approximation reduces the dominant computational cost to the Cholesky factorization of the $(M \times M)$ matrix $\tilde{\mathbf{K}}_{bb}$, which scales as $\mathcal{O}(M^3)$, and a factor $\mathcal{O}(LMD)$ from matrix multiplication. Consequently, the prior evaluation cost becomes linear in L .

Estimation. Parameter estimation in Stage 1 aims to achieve $\tilde{z}_i = (\mathcal{H}_i^{\beta_i} \circ \mathcal{G}_i^{\zeta_i})(y_i) \sim \mathcal{N}(0, 1)$, $i = 1, \dots, L$, where we write $\mathcal{H}_i^{\beta_i}$ to explicitly denote the dependence of \mathcal{H}_i on the parameters β_i . To further ease notation, we suppress the dependence of β_i and β on \mathbf{u} (cf. (9)). The same convention applies to \mathcal{G}_i and ζ_i . We employ a working independence assumption (which is dropped in Stage 2), constructing an auxiliary joint density

$$p(\mathbf{y}|\zeta, \beta) = \prod_{i=1}^L \left((\phi \circ \mathcal{H}_i^{\beta_i} \circ \mathcal{G}_i^{\zeta_i})(y_i) \times \left| \frac{\partial \mathcal{H}_i^{\beta_i}(\tilde{y}_i)}{\partial \tilde{y}_i} \right| \times \left| \frac{\partial \mathcal{G}_i^{\zeta_i}(y_i)}{\partial y_i} \right| \right), \quad (10)$$

where ϕ denotes the standard Gaussian density and $\tilde{y}_i = \mathcal{G}_i(y_i|\zeta_i)$. Given N independent replicates \mathbf{y}_j , $j = 1, \dots, N$, we apply gradient ascent to obtain joint maximum a posteriori (MAP) point estimates of the parameters and hyperparameters:

$$(\hat{\zeta}, \hat{\beta}, \hat{\boldsymbol{\theta}}^{\mathcal{G}}, \hat{\boldsymbol{\theta}}^{\mathcal{H}}) = \arg \max_{\zeta, \beta, \boldsymbol{\theta}^{\mathcal{G}}, \boldsymbol{\theta}^{\mathcal{H}}} \left(\prod_{j=1}^N p(\mathbf{y}_j|\zeta, \beta) \right) \left(\prod_{p=1}^P p(\zeta_p|\boldsymbol{\theta}_p^{\mathcal{G}}) \right) p(\beta|\boldsymbol{\theta}^{\mathcal{H}}). \quad (11)$$

For most covariance functions, each $\boldsymbol{\theta}_p^{\mathcal{G}}$, $p = 1, \dots, P$, and $\boldsymbol{\theta}^{\mathcal{H}}$ will consist of a length scale ℓ and an amplitude τ (omitting any indices), both of which are restricted to the positive real line. We therefore use softplus transformations $\ell = \ln(1 + \exp(\eta_{\ell}))$ and $\tau^2 = \ln(1 + \exp(\eta_{\tau}))$ and optimize over the real-valued parameters η_{ℓ} and η_{τ} using constant (uniform) priors. On the levels of ℓ and τ^2 , this implies improper priors that concentrate probability mass near zero but have a heavy right tail. See [Appendix B](#) for more details.

3.2. Stage 2: Estimation of the transport map \mathcal{T}

In the second stage, we fix the marginal transformations using the Stage 1 estimates to obtain pseudo-data $\hat{\mathbf{z}} = (\mathcal{H}^{\hat{\beta}} \circ \mathcal{G}^{\hat{\zeta}})(\mathbf{y})$. Estimation aims to achieve $\mathcal{T}(\hat{\mathbf{z}}) \sim \mathcal{N}(\mathbf{0}, \mathbf{I})$, such that the

second-stage joint density is

$$p(\hat{\mathbf{z}}) = \prod_{i=1}^L \left(\phi(\mathcal{T}_i(\hat{\mathbf{z}}_{1:i})) \times \left| \frac{\partial \mathcal{T}_i(\hat{\mathbf{z}}_{1:i})}{\partial \hat{\mathbf{z}}_i} \right| \right). \quad (12)$$

This allows us to directly apply the empirical Bayes estimation approach developed by Katzfuss and Schäfer (2023), which we briefly summarize here. Through \mathcal{T}_i , the joint density (12) depends on f_i and d_i^2 ; $i = 1, \dots, L$, which in turn depend on the hyperparameters $\boldsymbol{\theta}^\mathcal{T}$ as described in Subsection 2.7. We collect the sample of N pre-transformed observations $\hat{\mathbf{z}}_j$ in a $N \times L$ matrix $\hat{\mathbf{Z}} = (\hat{\mathbf{z}}_1, \dots, \hat{\mathbf{z}}_N)^\top$, with row j holding realization $\hat{\mathbf{z}}_j$ for all $j = 1, \dots, N$. Proposition 2 in Katzfuss and Schäfer (2023) gives an expression for the marginal likelihood $p(\hat{\mathbf{Z}}|\boldsymbol{\theta}^\mathcal{T})$ with the f_i and d_i^2 integrated out. We maximize this marginal likelihood using gradient-based optimization to find $\hat{\boldsymbol{\theta}}^\mathcal{T} = \arg \max_{\boldsymbol{\theta}^\mathcal{T}} p(\hat{\mathbf{Z}}|\boldsymbol{\theta}^\mathcal{T})$. Given $\boldsymbol{\theta}^\mathcal{T}$, we obtain the elements of the posterior transport map by Proposition 1 in Katzfuss and Schäfer (2023) in closed form. The scalability of estimation for \mathcal{T} is improved by a Vecchia-type approximation (Katzfuss & Guinness, 2021; Kidd & Katzfuss, 2022), making the simplifying assumption that f_i depends on a subset of the elements of $\tilde{\mathbf{z}}_{<i}$ instead of the full vector: $f_i(\tilde{\mathbf{z}}_{<i}) = f_i(\tilde{\mathbf{z}}_{c(i)})$ for some $c(i) \subseteq \{1, \dots, i-1\}$. The size of the conditioning set $c(i)$ is based on the relevance decay in the prior for f_i , such that only relevant elements of $\tilde{\mathbf{z}}_{<i}$ are included. Specifically, the maximum size of $c(i)$ is set to $m = \max\{j \geq 1 : \exp(-j \exp(\theta^a)) \geq \epsilon\}$, with $\epsilon = 0.01$. This reduces the computational complexity for determining the i^{th} element of the posterior map from $\mathcal{O}(N^3 + iN^2)$ to at most $\mathcal{O}(N^3 + mN^2)$, with m typically < 10 .

3.3. Computational complexity

Assuming $L > M > N > D > m > P$, the overall time complexity of a single evaluation of the unnormalized log posterior in our approach can be summarized as $\mathcal{O}(LD(M+N) + M^3P)$ for our marginal model and $\mathcal{O}(LN^3)$ for the BTM dependence model. Inverse evaluations scale linearly in NL except for the transport map inversion, which introduces a quadratic dependence on N per recursion step. For optimization, gradients are obtained via automatic differentiation in JAX (DeepMind et al., 2020), so gradient evaluations scale like log-posterior evaluations up to a constant-factor overhead. In typical applications, the overall runtime is primarily driven by operations linear in NL and cubic in N (which is typically small). A detailed summary of all computational costs is provided in Appendix C, Table 1.

4. Emulating internal climate variability

4.1. Climate data and comparison set-up

We demonstrate our method’s capacity to emulate high-dimensional climate fields using log-transformed total precipitation rate data from the Community Earth System Model (CESM) Large Ensemble Project (Kay et al., 2015), as mentioned in the introduction. While CESM simulates the full climate system, generating large ensembles of a single target field, such as precipitation, still requires the full computational cost of the underlying model, on the order of 10^5 CPU hours per ensemble member. Thus, a data-efficient stochastic surrogate offers immense scientific value. Recall that the data reside on a roughly 1° longitude-latitude global grid of size $L = 288 \times 192 = 55,296$. We use 98 samples, representing model outputs for consecutive years starting in the year 402. The grid is trimmed at the poles to remove duplicate locations, yielding a field of size $L = (288 \times 190) + 2 = 54,722$ for practical use.

We evaluate several variants of our scalable composite transformations (SCT) model against state-of-the-art baselines:

nonlin TM: Fixes both marginal transformation layers to the identity map, yielding the non-linear Bayesian transport map as proposed by Katzfuss and Schäfer (2023).

SCT-Gauss: \mathcal{G}_i is defined with components $\mathcal{G}_i(y_i) = \Phi^{-1}(\Phi(y_i|\mu_i, \sigma_i^2)) = (y_i - \mu_i)/\sigma_i$, i.e. using a Gaussian distribution with mean and variance varying over locations. We estimate the inverse softplus transformations of the standard deviations, $\eta_i = \ln(\exp(\sigma_i) - 1)$, such that we have $\zeta_i = (\mu_i, \eta_i)$.

SCT-Skew-t: \mathcal{G}_i is defined with components $\mathcal{G}_i(y_i) = \Phi^{-1}(F(y_i|\mu_i, \sigma_i, \alpha_i, \nu))$, where F is the CDF of a Type-3 skewed t -distribution (see Rigby et al., 2020) with location $\mu_i \in \mathbb{R}$, scale $\sigma_i \in \mathbb{R}_{>0}$, skewness $\alpha_i \in \mathbb{R}_{>0}$, and degrees of freedom $\nu \in \mathbb{R}_{>0}$. With $\alpha_i = 1$, the symmetric t -distribution is retrieved; with $\alpha_i > 1$ and $0 < \alpha_i < 1$, the distribution becomes right- and left-skewed, respectively. We estimate the positive-valued parameters on inverse-softplus level, $\eta = \ln(\exp(\cdot) - 1)$, such that we have $\zeta_i = (\mu_i, \eta_{\sigma_i}, \eta_{\alpha_i}, \eta_{\nu})^T$. The degrees of freedom ν do not vary across locations.

We assess each configuration with and without the semi-parametric correction layer \mathcal{H} . When active, \mathcal{H} uses a global random-walk variance τ^2 , boundaries $a = -b = -4$, and $D = 40$ flexible parameters. In all models, the transport map \mathcal{T} is defined as in Subsection 2.7.

We evaluate the models based on their predictive performance using log scores, given by the negative expectation of the log predictive density $-\mathbb{E}_{\mathbf{y}^*}[\ln p(\mathbf{y}^*|\mathbf{Y})]$ for a new test field \mathbf{y}^* . This log score is equivalent (up to an additive constant) to the Kullback-Leibler divergence between the unknown true distribution and the model’s approximation. We evaluate the predictive density by plugging the point estimates for the parameters of \mathcal{G} and \mathcal{H} into (5), and using the posterior predictive transport map given $\hat{\theta}^{\mathcal{T}}$. We approximate the expectation by averaging over 14 holdout replications not used for either estimation or early stopping, and over five random train/test splits.

4.2. Americas subregion

First, we consider a subset of the full field of size $L = 37 \times 74 = 2,738$ in a region containing parts of the Americas (30°S to 40°N and 115°W to 70°W). This subset allows for performance comparisons to alternative approaches that do not scale well to the full global dataset. These include **local**, a locally parametric method for climate data that fits anisotropic Matérn covariances in local windows and combines the local fits into a global model (Wiens et al., 2020), **MatCov**, a Gaussian model with zero mean and isotropic Matérn covariance, **linear TM**, a simplified version of \mathcal{T} that sets all map elements to linear functions, and **DPM**, a version of \mathcal{T} that incorporates a Dirichlet process mixture model to allow non-Gaussian distributions for the errors ϵ_i in the nonlinear regressions $\tilde{z}_i = f_i(\tilde{\mathbf{z}}_{<i}) + \epsilon_i$ of the map elements. In Katzfuss and Schäfer (2023), DPM showed the best predictive performance on the Americas data, but since it requires MCMC sampling, it does not scale well to large spatial fields.

Our results for the Americas subregion are shown in panel a) of Figure 5. We use $M = 64$ inducing locations for the low-rank approximations in the marginal models. For all considered composite models, estimating the semi-parametric correction dramatically improves predictive performance even with small sample sizes. The best overall performance is obtained by the model with semi-parametric correction and skew- t marginal. All of our full composite transformation models outperform DPM (and all other competitors). Remarkably, **SCT-Skew-t** achieves a better log score with $N_{\text{train}} = 20$ than the previous state-of-the-art (DPM) achieves with $N_{\text{train}} = 80$. The scores taken from Katzfuss and Schäfer (2023) are shifted to correct for different preprocessing, see Appendix D for details.

Figure 6 contrasts the standardized marginal distributions of the CESM data against samples from **SCT-Skew-t** ($N_{\text{train}} = 20$) and **nonlin TM** ($N_{\text{train}} = 80$) at five areas in the Americas. The data (row a) exhibit similar distributional features at neighboring locations but significant spatial heterogeneity across the five areas, ranging from near-Gaussian (Location 1) to pronounced

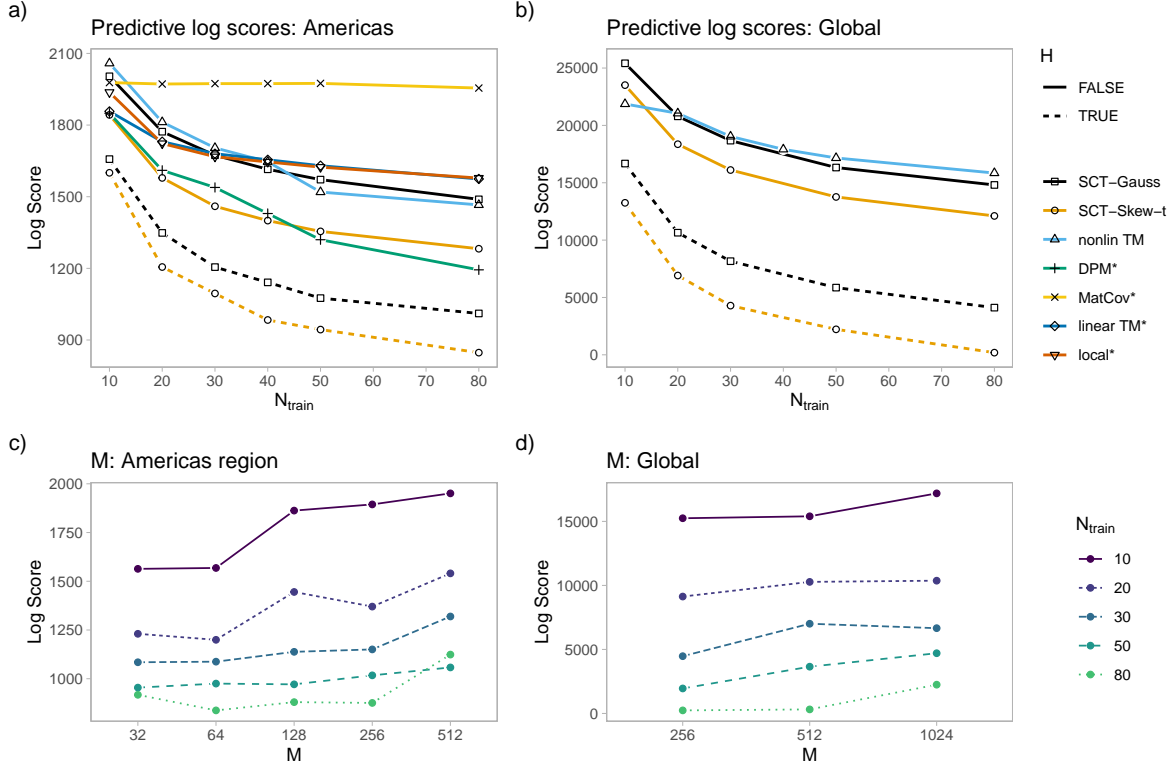


Figure 5 Our SCT models are substantially more accurate climate emulators than existing methods in terms of log scores (lower is better). The top row shows average predictive log scores over five random train/test splits. Dashed lines indicate models that include a fitted semi-parametric correction layer \mathcal{H} . Results marked with an asterisk (*) are taken from Katzfuss and Schäfer (2023), Fig. 10, without re-running the models. The bottom row shows predictive log scores in the SCT-Skew-t specification (including a fitted semi-parametric layer \mathcal{H}) as a function of the number of inducing points M and training samples N_{train} .

skewness (Location 3) and multimodality (Location 4). Despite using only $N_{\text{train}} = 20$ replicates, SCT-Skew-t (row b) faithfully reproduces these complex features, capturing the heavy tails and bimodal structures that characterize the local precipitation regimes. Conversely, the nonlin TM (row c)—even with $N_{\text{train}} = 80$ —reverts to a Gaussian-like profile, effectively smoothing out the local asymmetries and extremes essential for accurate risk quantification.

4.3. Global data

For the global dataset, we observe the same pattern in log scores as for the Americas, see Figure 5 b). We use $M = 256$ for the SCT models. Since DPM is not viable for the full global dataset, we consider nonlin TM as the state-of-the-art benchmark. Most notably, SCT-Skew-t substantially outperforms nonlin TM, yielding a lower log score using $N_{\text{train}} = 10$ than nonlin TM achieves using $N_{\text{train}} = 80$. By reducing the training requirement from 80 to 10 runs, our method effectively provides an eight-fold increase in the computational budget for climate research, allowing scientists to explore eight times as many emission scenarios for the same cost.

In Figure 7, we compare samples for the global grid generated from the physical climate model (left column, labeled *CESM Output 1* and *2*) to samples from SCT-Skew-t and nonlin TM, trained on $N_{\text{train}} = 20$ and $N_{\text{train}} = 80$ field samples. Consistent with the quantitative log-score results, the SCT-Skew-t model produces samples that look qualitatively similar to the CESM output, reproducing both the large-scale and small-scale spatial structure, even when trained on only 20 examples. Increasing N_{train} to 80 refines the representation without substantially

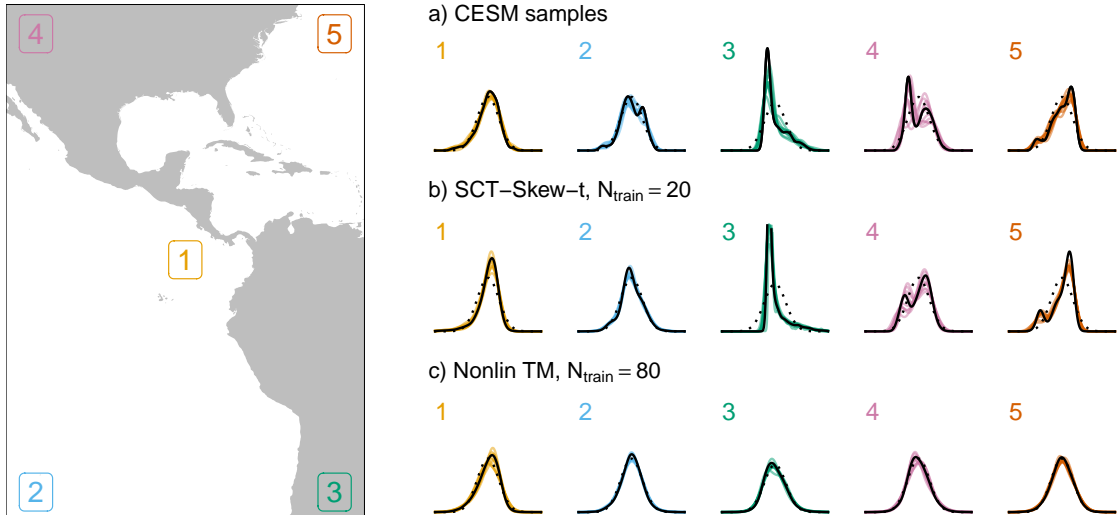


Figure 6 Marginal distributions at and near five locations in the Americas region. The selected locations are the first five locations of a maximin ordering of all locations in the region. Each numbered panel shows data for the respective location and the nine closest locations. The solid black lines show kernel density estimates obtained from pooling the data from all ten locations. The colored lines show kernel density estimates of the data at the individual locations. The dotted line is a standard Gaussian density for reference. Row a) uses all 98 replicates in the data, row b) uses 1000 samples from `SCT-Skew-t` trained on $N_{\text{train}} = 20$ replicates, and row c) uses 1000 samples from `nonlin TM` trained on $N_{\text{train}} = 80$ replicates.

altering the overall appearance. `Nonlin TM` also reproduces the main large-scale features of the CESM data, but its samples exhibit noticeably stronger contrasts and more pronounced regional patterns than those present in the CESM output. This becomes particularly apparent when contrasting `SCT-Skew-t` at $N_{\text{train}} = 20$ with `nonlin TM` at $N_{\text{train}} = 80$: despite having considerably more training data, the `nonlin TM` sample still exhibits amplified variation, while `SCT-Skew-t` already provides a close visual match to the CESM output’s distribution with far fewer training cases.

Figure 8 compares the spatial distribution of severe rainfall (Panel a) and dry conditions (Panel b) across the CESM samples and the two surrogate models. In both cases, `SCT-Skew-t` trained on only $N_{\text{train}} = 20$ fields (middle column) reproduces the spatial structure visible in the CESM data better than `nonlin TM` trained on $N_{\text{train}} = 80$. The probability of severe rainfall is overestimated by `nonlin TM` across large areas including North America, Europe, Russia, and equatorial Africa. In contrast, `SCT-Skew-t` shows less pronounced overestimation, which is further reduced with increased training sample size (not shown). Considering dry conditions, `nonlin TM` underestimates the probability of low precipitation, while `SCT-Skew-t` closely reproduces both the spatial pattern and the relative magnitude of low-precipitation probabilities. These results corroborate the quantitative results in terms of improved log-scores, suggesting that inferences drawn from `SCT-Skew-t` tend to be more consistent than `nonlin TM` with the mechanisms underlying the data-generating precipitation process, even in small-data settings.

Inducing locations and runtime. Panels c) and d) of **Figure 5** compare predictive log scores from `SCT-Skew-t` when using different numbers of inducing locations M for the Americas data (c) and the whole global grid (d). In both cases, there is no indication of performance improvements to be gained from using more inducing locations; in fact, performance appears to worsen slightly when $M > 64$ for the Americas and $M > 256$ for the global grid. This is likely a result of the division of labor between the marginal and the dependence model

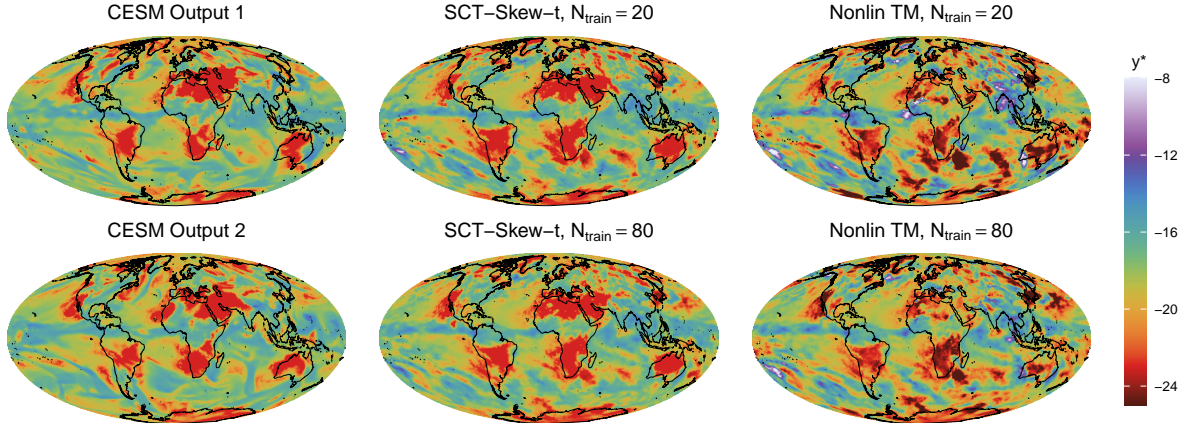


Figure 7 Comparison of climate-model output (left column) to samples from `SCT-Skew-t` including \mathcal{H} (middle column) and `nonlin TM` (right column). Ideally, the surrogate samples should look like they are drawn from the same distribution as the climate-model output. To facilitate comparisons between the samples from the surrogate models, all samples in the right four panels are generated by inverting the transformations on the same random noise realization \mathbf{z}^* drawn from $\mathcal{N}(\mathbf{0}, \mathbf{I})$. To keep the color scale in a reasonable range, we truncate the data to $[-25, -8]$, which is relevant mainly for the samples from `nonlin TM`.

parts: the marginal models, where the inducing locations are relevant, can benefit from the regularizing effect of a high degree of spatial smoothness, as implied by low numbers of inducing points, because the dependence model is well-equipped to capture fine-scale local dependencies in the data. As larger M also substantially increases the computational cost, we use $M = 256$ when analyzing the global data. Then, one optimization step takes about 0.7 (0.36) seconds $N_{\text{train}} = 80$ ($N_{\text{train}} = 10$), which is insignificant compared to the time cost of about 6 (0.6) seconds per iteration for the dependence model \mathcal{T} at $N_{\text{train}} = 80$ ($N_{\text{train}} = 10$). The timing results were obtained on a 14 inch 2021 M1 MacBook Pro using the `SCT-Gauss` configuration including \mathcal{H} for the marginal model as described above. Remarkably, our full emulator can be trained in minutes on this standard laptop, a negligible carbon footprint compared to the thousands of core-hours required for the original climate simulations.

5. Conclusions

We have proposed a scalable generative framework for emulating the internal variability of high-dimensional, non-Gaussian climate fields that effectively overcomes the data scarcity inherent in climate emulation. By composing flexible marginal layers with a sparse Bayesian transport map, our method decouples the estimation of heavy-tailed marginal features from complex spatial dependencies. Crucially, our results demonstrate that this architectural choice allows for “high-fidelity emulation on a budget”: achieving state-of-the-art accuracy with 87.5% less training data than existing methods. For climate science, this efficiency effectively octuples the computational budget, enabling richer ensemble analyses of tail risks without additional supercomputing costs. While applied to global precipitation fields here, the approach is broadly applicable to any massive multivariate setting where data is expensive but structured—including temporal, spatio-temporal, or network-based contexts amenable to distance-based ordering.

A natural direction for extending the model is the inclusion of physical drivers (e.g., global mean temperature, emissions levels) or other covariates in the marginal layers, for instance through generalized additive models for location, scale, and shape (Rigby & Stasinopoulos, 2005). Another important avenue concerns the estimation procedure. Our two-step empirical-Bayes approach offers a favorable balance between predictive accuracy and computational cost,

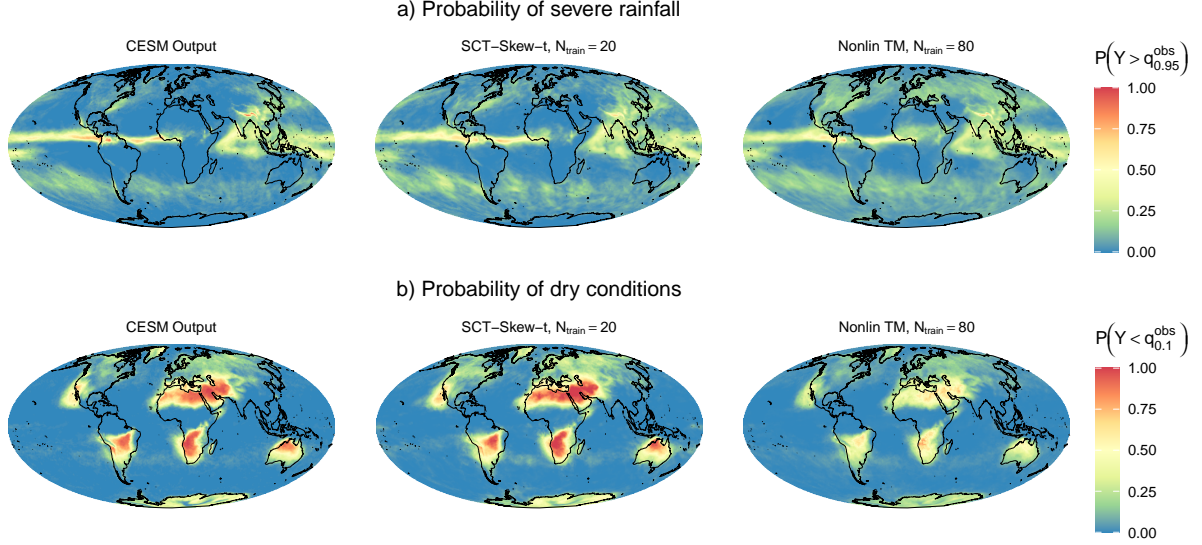


Figure 8 Comparison of location-wise probability of wet (row a) and dry (row b) conditions, defined as log precipitation rates above the 0.95 and below the global 0.1 quantile of all 98 fields in the CESM data, respectively ($q_{0.95}^{\text{obs}} \approx -15.81$ and $q_{0.1}^{\text{obs}} \approx -22.78$). We compare the probabilities in the full CESM data (left) to SCT-Skew-t trained on 20 fields (middle) and `nonlin` TM trained on 80 fields (right).

but it does not propagate uncertainty from the marginal layers to the dependence model. Developing scalable strategies for uncertainty propagation or approximating the full joint posterior through variational inference could further improve predictive performance. Overall, our proposed framework of scalable composite transformations provides a flexible basis for modeling complex multivariate distributions, and we anticipate that it will support a wide range of future applications.

Acknowledgments

MK and PFVW were partially supported by NASA’s Advanced Information Systems Technology Program (AIST-21). MK’s research was also partially supported by National Science Foundation (NSF) Grant DMS-1953005 and by the Office of the Vice Chancellor for Research at the University of Wisconsin–Madison with funding from the Wisconsin Alumni Research Foundation. JB was partially supported by a scholarship from the German Academic Exchange Service (DAAD) and by the German Research Foundation (DFG) through grant 443179956. We would like to thank Felix Jimenez and Mark Risser for helpful comments and discussions.

A. Proofs

Lemma 1 (\mathcal{H}_i passes through k_1). *The function $\mathcal{H}_i(\cdot|\beta_i)$ fulfills $\mathcal{H}_i(k_1|\beta_i) = k_1$ for all $\beta_i \in \mathbb{R}^D$.*

Proof. Due to the localized definition of B-splines, the only nonzero basis functions in $\mathcal{H}_i(k_1|\beta_i)$ are B_1 , B_2 , and B_3 . Using this fact, and inserting our definitions $k_0 = \gamma_{1,i}$ and $k = \exp(\gamma_{i,j})$ for $j \in \{2, 3\}$, we can write $\mathcal{H}_i(k_1|\beta_i) = \sum_{j=1}^3 B_j(k_1) \left(k_0 + \sum_{i=2}^j k \right)$. Now observe that, for any $x \in [k_1, k_m]$, B-splines have the property of unity decomposition, meaning that $\sum_{j=1}^J B_j(x) = 1$. Since only the first three bases are nonzero when evaluating at k_1 , this implies that $\sum_{j=1}^3 B_j(k_1) = 1$, such that we can simplify to $\mathcal{H}_i(k_1|\beta_i) = k_0 + k \sum_{j=1}^4 B_j(k_1)j - k$. By way of the recursive definition of B-spline bases (Fahrmeir et al., 2013, p. 429), we can now see that we have $\sum_{j=1}^4 B_j(k_1)j = 2$, such that $\mathcal{H}_i(k_1|\beta_i) = k_0 + k = k_1$ as desired. \square

Lemma 2 (Unit slope on $[k_1, a]$ and $[b, k_m]$). *For any $x \in [k_1, a]$, the function $\mathcal{H}_i(\cdot|\beta_i)$ fulfills $\frac{\partial}{\partial x} \mathcal{H}_i(x|\beta_i) = 1$ for all $\beta_i \in \mathbb{R}^D$.*

Proof. By Lemma B.1 in Brachem et al. (2025), the derivative of $\mathcal{H}_i(x|\beta_i)$ for $x \in [k_1, a]$ can be written as $\frac{\partial}{\partial x} \mathcal{H}_i(x|\beta_i) = \sum_{j=2}^4 B_j^{(2)}(x) \exp(\gamma_j)/k$, where $B_j^{(2)}$ denotes bases of order two, and we assume the same knot sequence as above. Inserting $\exp(\gamma_j) = k$ for $j \in \{2, 3, 4\}$, we note that $\frac{\partial}{\partial x} \mathcal{H}_i(x|\beta_i) = \sum_{j=2}^4 B_j^{(2)}(x) = 1$ for

any $x \in [k_1, a]$, by the unity decomposition property of B-spline bases. The proof for $x \in [b, k_m]$ is completely analogous. \square

Lemma 3 (Average slope of one over $[a, b]$). *The function $\mathcal{H}_i(x|\beta_i)$ has an average slope of one over the interval $x \in [a, b]$, i.e. for all $\beta_i \in \mathbb{R}^D$ it fulfills $\frac{1}{b-a} \int_a^b \frac{\partial}{\partial x} \mathcal{H}_i(x|\beta_i) dx = 1$.*

Proof. To reduce notational burden, we suppress the location index i for the coefficients β and γ in this proof, which can be done without loss of generality. By Lemma B.2 in the appendix of Brachem et al. (2025), the average derivative in a segment $x \in [k_j, k_{j+1}]$ of a monotonically increasing B-spline defined on equidistant knots as given in (6) is known in closed form as

$$\frac{1}{k} \int_{k_j}^{k_{j+1}} \frac{\partial}{\partial x} \mathcal{H}_i(x) dx = \frac{1}{k} \left(\frac{1}{6} \exp(\gamma_{j+1}) + \frac{2}{3} \exp(\gamma_{j+2}) + \frac{1}{6} \exp(\gamma_{j+3}) \right). \quad (13)$$

Since $a = k_2$ and $b = k_{m-1}$, we can obtain the average slope over the interval $[a, b]$ by averaging over the local averages of all function segments $[k_j, k_{j+1}]$ for $j = 2, 3, \dots, m-2$:

$$\frac{1}{b-a} \int_a^b \frac{\partial}{\partial x} \mathcal{H}_i(x) dx = \frac{1}{k_{m-1} - k_2} \int_{k_2}^{k_{m-1}} \frac{\partial}{\partial x} \mathcal{H}_i(x) dx \quad (14)$$

$$= \frac{1}{k(m-3)} \sum_{j=2}^{m-2} \int_{k_j}^{k_{j+1}} \frac{\partial}{\partial x} \mathcal{H}_i(x) dx \quad (15)$$

$$= \frac{1}{k(m-3)} \sum_{j=2}^{m-2} \left(\frac{1}{6} \exp(\gamma_{j+1}) + \frac{2}{3} \exp(\gamma_{j+2}) + \frac{1}{6} \exp(\gamma_{j+3}) \right) \quad (16)$$

$$= \frac{1}{k(m-3)} \left(2k + \sum_{j=5}^{J-3} \exp(\gamma_j) \right). \quad (17)$$

Note that $k_{m-1} - k_2 = k(m-3)$. For rearranging the sum on the last line, we observe that we fixed $\gamma_{i,j} = \log(k)$ for $j \in \{2, 3, 4\} \cup \{J-2, J-1, J\}$. The simplified sum on the last line then becomes possible by making use of the fact that the sum contains the terms $\exp(\gamma_3)/6 + 2\exp(\gamma_4)/3 + \exp(\gamma_4)/6 = k$ and $\exp(\gamma_{J-1})/6 + 2\exp(\gamma_{J-2})/3 + \exp(\gamma_{J-2})/6 = k$. For the remaining $\gamma_5, \gamma_6, \dots, \gamma_{J-3}$, the fractions sum up to one. Now recall that, for $j \in \{5, 6, \dots, J-3\}$, we have defined $\gamma_j = \beta_{j-4} - \log\left(\left((m-5)k\right)^{-1} \sum_{d=1}^D \exp(\beta_{i,d})\right)$, with $\beta_d \in \mathbb{R}$ for $d = 1, \dots, D$ and $D = J-7$. We can thus write

$$\sum_{j=5}^{J-3} \exp(\gamma_j) = \sum_{d=1}^D \exp\left(\beta_{i,d} - \log\left(\frac{\sum_{d=1}^D \exp(\beta_{i,d})}{(m-5)k}\right)\right) \quad (18)$$

$$= \sum_{d=1}^D \exp(\beta_{i,d}) \left(\frac{(m-5)k}{\sum_{d=1}^D \exp(\beta_{i,d})}\right) \quad (19)$$

$$= (m-5)k \quad (20)$$

and insert this expression back to arrive at $(b-a)^{-1} \int_a^b \frac{\partial}{\partial x} \mathcal{H}_i(x) dx = (k(m-3))^{-1} k(m-5+2) = 1$, which concludes the proof. \square

Lemma 4 (\mathcal{H}_i passes through a and b). *The function $\mathcal{H}_i(\cdot|\beta_i)$ fulfills $\mathcal{H}_i(a|\beta_i) = a$ and $\mathcal{H}_i(b|\beta_i) = b$ for all $\beta_i \in \mathbb{R}^D$.*

Proof. By Lemma 1, we have $\mathcal{H}_i(k_1|\beta_i) = k_1$, and by Lemma 2, the slope of $\mathcal{H}_i(x|\beta_i)$ for all $x \in [k_1, a]$ is one. As result, we directly get $\mathcal{H}_i(a|\beta_i) = a$. Further, by Lemma 3, the average slope of $\mathcal{H}_i(x|\beta_i)$ over the interval $[a, b]$ is one, which, given that $\mathcal{H}_i(a|\beta_i) = a$ as we just noted, implies that $\mathcal{H}_i(b|\beta_i) = b$. \square

Proposition 1 (\mathcal{H}_i is identity outside a compact set). *The function \mathcal{H}_i fulfills $\mathcal{H}_i(\tilde{y}_i|\beta_i) = \tilde{y}_i$ for all $\tilde{y}_i \in (-\infty, a] \cup [b, \infty)$ and for all $\beta_i \in \mathbb{R}^D$.*

Proof of Proposition 1. By Lemma 4, we have $\mathcal{H}_i(a|\beta_i) = a$ and $\mathcal{H}_i(b|\beta_i) = b$, and by Lemma 2, $\mathcal{H}_i(x|\beta_i)$ has a unit slope for all $x \in [k_1, a] \cup [b, k_m]$. This means that $\mathcal{H}_i(x|\beta_i) = x$ for all $x \in [k_1, a] \cup [b, k_m]$. The statements above all hold for all $\beta_i \in \mathbb{R}^D$. Since $\mathcal{H}_i(x|\beta_i) = x$ for $x < k_1$ and $x > k_m$ by definition, this concludes the proof. \square

From a technical perspective, this result is important, because it shows that the transformation function's transition back to identity at both tails happens in the B-spline function segment, which means in turn that the transition is continuous and twice continuously differentiable, and that the function as a whole is continuous and twice continuously differentiable. From a modeling perspective, it is important, because it allows us to think

of \mathcal{H}_i as a flexible increasing B-spline on (a, b) that transitions smoothly to the identity function beyond the flexible subdomain. Since \mathcal{H}_i is a strictly monotonically increasing B-spline on $[k_1, k_m]$ by construction, this proposition also implies that $\mathcal{H}_i(\tilde{y}_i|\beta_i)$ is strictly monotonically increasing in \tilde{y}_i for all $\tilde{y}_i \in \mathbb{R}$ and $\beta_i \in \mathbb{R}^J$. Further, it allows us to note that the derivative of $\mathcal{H}_i(\tilde{y}_i|\beta_i)$ with respect to \tilde{y}_i is a second-order B-spline $(\partial/\partial\tilde{y}_i)\mathcal{H}_i(\tilde{y}_i|\beta_i) = \sum_{j=2}^J B_j^{(2)}(\tilde{y}_i) \exp(\gamma_j)/k$ for $\tilde{y}_i \in [k_1, k_m]$ and 1 else, where $B_j^{(2)}$ are second-order B-spline bases defined on the same knots as (6). Note that $(\partial/\partial\tilde{y}_i)\mathcal{H}_i(\tilde{y}_i|\beta_i)$ depends on β_i through $\gamma_5, \dots, \gamma_{J-3}$ as given in (7).

Proof of Theorem 1. We can use the identities $\beta_{1,i} = \beta_{2,i} = \dots = \beta_{D,i} = \beta_i$ to simplify the definition of $\gamma_{j,i}$ for $j \in \{5, 6, \dots, J-3\}$ to $\gamma_{j,i} = \log(m-5) - \log(D) + \log(k)$. Since $m = D+5$, this expression reduces to $\gamma_{j,i} = \log(k)$, such that we now have $\gamma_{j,i} = \log(k)$ for all $j = 2, \dots, J$. This allows us to apply Lemma 2 separately to all function segments $[k_j, k_{j+1}]$ for $j = 1, \dots, m-1$, showing that $\mathcal{H}_i(x|\beta_i)$ has a constant unit slope for all $x \in [k_1, k_m]$. When combining this observation with Proposition (1), which shows that $\mathcal{H}_i(x|\beta_i)$ is the identity function for $x \in (-\infty, k_2] \cup [k_{m-1}, \infty)$, the proof is complete. \square

Proof of Theorem 2. Since both \mathcal{H}_i and \mathcal{G}_i are strictly monotonically increasing, the assumption $(\mathcal{H}_i \circ \mathcal{G}_i)(y_i) \sim \mathcal{N}(0, 1)$ implies that $\mathbb{P}(y_i \leq t) = \mathbb{P}((\mathcal{H}_i \circ \mathcal{G}_i)(y_i) \leq (\mathcal{H}_i \circ \mathcal{G}_i)(t)) = (\Phi \circ \mathcal{H}_i \circ \mathcal{G}_i)(c)$. Further, since $t \in (-\infty, q_a] \cup [q_b, \infty)$, we have $\mathcal{G}_i(t) \in (-\infty, a] \cup [b, \infty)$. Applying Proposition 1, this means that $(\mathcal{H}_i \circ \mathcal{G}_i)(t) = \mathcal{G}_i(t)$, which now allows us to write $\mathbb{P}(y_i \leq t) = (\Phi \circ \mathcal{G}_i)(t) = (\Phi \circ \Phi^{-1} \circ F_i)(t) = F_i(t)$, by substituting the definition of \mathcal{G}_i . \square

B. Improper prior induced by a flat inverse-softplus parameterization

Let $\eta \in \mathbb{R}$ and define

$$\tau^2 = \text{softplus}(\eta)^2 = \log(1 + \exp(\eta))^2, \quad \tau > 0.$$

Assume an (improper) constant prior on the latent variable, $p(\eta) \propto 1$. The inverse transformation is

$$\eta = \ln(\exp(\tau) - 1),$$

with derivative

$$\frac{d\eta}{d\tau} = \frac{\exp(\tau)}{\exp(\tau) - 1} = \frac{1}{1 - \exp(-\tau)}.$$

By change of variables, the induced improper prior on τ is therefore

$$p(\tau) \propto \left| \frac{d\eta}{d\tau} \right| = \frac{1}{1 - \exp(-\tau)}, \quad \tau > 0,$$

and the induced improper prior on τ^2 is

$$p(\tau^2) \propto p(\tau) \left| \frac{d\tau}{d\tau^2} \right| = \frac{1}{1 - \exp(-\sqrt{\tau^2})} \frac{1}{2\sqrt{\tau^2}}, \quad \tau > 0.$$

As $\tau^2 \rightarrow 0$, we also have $\tau \rightarrow 0$, and consequently $\exp(-\tau) \rightarrow 1$. Thus, in the improper prior above, both fractions become large as $\tau^2 \rightarrow 0$, such that small values of τ^2 are favored by this prior. At the same time, as $\tau^2 \rightarrow \infty$, we have $\exp(-\tau) \rightarrow 0$, so that the left fraction tends to 1. Then, for any $a \in \mathbb{R}$, the tail probability mass implied by this prior as $\tau^2 \rightarrow \infty$ is

$$\int_a^\infty p(\tau^2) d\tau^2 \geq \int_a^\infty \frac{1}{2\sqrt{\tau^2}} d\tau^2 = \infty,$$

which diverges. In summary, the flat prior on $\eta = \ln(\exp(\tau) - 1)$ induces an improper prior on τ and τ^2 that strongly favors small variances, but only weakly penalizes large variances due to a heavy right tail.

C. Dominant computational costs

Table 1 summarizes the dominant computational complexity of the main model components assuming L locations, N independent samples of the full field, M inducing locations for the low-rank approximations in the marginal models, P parameters in each parametric marginal model \mathcal{G}_i , and D flexible spline-parameters in each semiparametric marginal model \mathcal{H}_i . Lower-order terms and constant factors are omitted. Spline evaluations in \mathcal{H} are accelerated using linear interpolation on a precomputed regular grid of size $G = 1000$, reducing basis-function evaluation to a binary search followed by interpolation. The derivative of the spline reuses the same grid and search results, so derivative evaluation introduces only an additional matrix multiplication and therefore has the same asymptotic dependence on N , L , and D . See Katzfuss and Schäfer (2023) for details on the transport map complexity. The semiparametric marginal layer is inverted numerically using cubic interpolation on a regular grid via the Python library Interpax (Conlin, 2025).

Assuming $L > M > N > D > m > \log G > P$, the overall time complexity of a single evaluation of the unnormalized log posterior is $\mathcal{O}(LD(M + N) + M^3P)$ for our marginal model and $\mathcal{O}(LN^3)$ for the BTM dependence model.

Table 1 Dominant computational complexity of the marginal model likelihood; m denotes the size of the conditioning set in the posterior transport map, see [Subsection 3.2](#). The overview assumes a Gaussian model for \mathcal{G} .

Component	Complexity
Marginal Model	
Prior for ζ (low-rank, whitened)	$\mathcal{O}(PM)$
Approximation of ζ	$\mathcal{O}(PLM + PM^3)$
Prior for β (low-rank, whitened)	$\mathcal{O}(DM)$
Approximation of β	$\mathcal{O}(LMD + M^3)$
Evaluation of \mathcal{G}	$\mathcal{O}(NL)$
Evaluation of $\partial\mathcal{G}/\partial y$	$\mathcal{O}(NL)$
Evaluation of \mathcal{H}	$\mathcal{O}(NL \log(G) + NLD)$
Evaluation of $\partial\mathcal{H}/\partial \tilde{y}$	$\mathcal{O}(NLD)$
Dependence Model	
Evaluation of Gaussian reference density	$\mathcal{O}(NL)$
Evaluation of $p(\hat{\mathbf{Z}} \theta^T)$	$\mathcal{O}(LN^3)$
Evaluation of $\tilde{\mathcal{T}}$	$\mathcal{O}(LN^3 + mN^2)$
Application of $\tilde{\mathcal{T}}$	$\mathcal{O}(L(N^2 + mN))$
Inversion	
Inverse \mathcal{G}^{-1}	$\mathcal{O}(NL)$
Inverse \mathcal{H}^{-1}	$\mathcal{O}(NL)$
Inverse transport map $\tilde{\mathcal{T}}^{-1}$	$\mathcal{O}(L(N^2 + mN))$

D. Adjusted log scores

In [Figure 5](#), we show log scores taken from [Figure 10](#) in [Katzfuss and Schäfer \(2023\)](#), but shift them for a fair comparison. This shift is necessary, because the authors applied their models to a version of the data that was preprocessed by centering and scaling at each location based on the location-specific sample mean and standard deviation of the full sample. This step somewhat resembles our definition of \mathcal{G} in [SCT-Gauss](#), but without spatial smoothing. Since the preprocessing step was invariant among the models compared by [Katzfuss and Schäfer \(2023\)](#) it could be ignored in the computation of the log scores. Here, however, we consider \mathcal{G} as an integral part of the model and therefore have to account for it in the computation of the log scores – consequently, we have to adjust the log scores for the alternative models by computing $-\mathbb{E}[p(\mathbf{y}^*|\mathbf{Y})] + \sum_{i=1}^L \ln s_i$, where s_i is the sample standard deviation over $y_{i,1}, \dots, y_{i,N}$ at location i and $-\mathbb{E}[p(\mathbf{y}^*|\mathbf{Y})]$ is the log score reported by [Katzfuss and Schäfer \(2023\)](#). The log scores reported for our model runs are similarly adjusted for our z-standardization preprocessing step, but note that our z-standardization does not use location-specific means and standard deviations, but the global mean and standard deviation of the training sample.

References

- Ayala, A., Drazic, C., Hutchinson, B., Kravitz, B., & Tebaldi, C. (2021). *Loosely conditioned emulation of global climate models with generative adversarial networks*. arXiv: 2105.06386 [physics]. <https://doi.org/10.48550/arXiv.2105.06386>
- Banerjee, S., Carlin, B. P., & Gelfand, A. E. (2014). *Hierarchical modeling and analysis for spatial data*. Chapman and Hall/CRC. <https://doi.org/10.1201/b17115>
- Besombes, C., Pannekoucke, O., Lapeyre, C., Sanderson, B., & Thual, O. (2021). *Producing realistic climate data with GANs*. <https://doi.org/10.5194/npg-2021-6>

- Brachem, J., Wiemann, P. F. V., & Kneib, T. (2025). *Bayesian penalized transformation models: Structured additive location-scale regression for arbitrary conditional distributions*. arXiv: 2404.07440v4 [stat]. <https://doi.org/10.48550/arXiv.2404.07440>
- Choi, I., Li, B., & Wang, X. (2013). Nonparametric Estimation of Spatial and Space-Time Covariance Function. *Journal of Agricultural, Biological, and Environmental Statistics*, 18(4), 611–630. Retrieved September 11, 2025, from <https://www.jstor.org/stable/26452886>
- Conlin, R. (2025). *Interpax*. <https://doi.org/10.5281/zenodo.17516709>
- DeepMind, Babuschkin, I., Baumli, K., Bell, A., Bhupatiraju, S., Bruce, J., Buchlovsky, P., Budden, D., Cai, T., Clark, A., Danihelka, I., Dedieu, A., Fantacci, C., Godwin, J., Jones, C., Hemsley, R., Hennigan, T., Hessel, M., Hou, S., ... Viola, F. (2020). *The DeepMind JAX ecosystem [Python libraries]*. <https://github.com/google-deepmind>
- Fahrmeir, L., Kneib, T., Lang, S., & Marx, B. (2013). *Regression - models, methods and applications*. Springer. <https://doi.org/10.1007/978-3-642-34333-9>
- Gelfand, A. E., & Schliep, E. M. (2016). Spatial statistics and Gaussian processes: A beautiful marriage. *Spatial Statistics*, 18, 86–104. <https://doi.org/10.1016/j.spasta.2016.03.006>
- Guinness, J. (2018). Permutation and grouping methods for sharpening Gaussian process approximations. *Technometrics*, 60(4), 415–429. <https://doi.org/10.1080/00401706.2018.1437476>
- Herp, M., Brachem, J., Altenbuchinger, M., & Kneib, T. (2024). *Graphical transformation models*. arXiv: 2503.17845. <https://doi.org/10.48550/arXiv.2503.17845>
- Hothorn, T., Möst, L., & Bühlmann, P. (2018). Most likely transformations. *Scandinavian Journal of Statistics*, 45(1), 110–134. <https://doi.org/10.1111/sjos.12291>
- Joe, H. (2005). Asymptotic efficiency of the two-stage estimation method for copula-based models. *Journal of Multivariate Analysis*, 94(2), 401–419. <https://doi.org/10.1016/j.jmva.2004.06.003>
- Katzfuss, M., & Guinness, J. (2021). A general framework for vecchia approximations of gaussian processes. *Statistical Science*, 36(1). <https://doi.org/10.1214/19-STS755>
- Katzfuss, M., & Schäfer, F. (2023). Scalable Bayesian transport maps for high-dimensional non-gaussian spatial fields. *Journal of the American Statistical Association*, 1–15. <https://doi.org/10.1080/01621459.2023.2197158>
- Kay, J. E., Deser, C., Phillips, A., Mai, A., Hannay, C., Strand, G., Arblaster, J. M., Bates, S. C., Danabasoglu, G., Edwards, J., Holland, M., Kushner, P., Lamarque, J.-F., Lawrence, D., Lindsay, K., Middleton, A., Munoz, E., Neale, R., Oleson, K., ... Vertenstein, M. (2015). The Community Earth System Model (CESM) large ensemble project: A community resource for studying climate change in the presence of internal climate variability. *Bulletin of the American Meteorological Society*, 96(8), 1333–1349. <https://doi.org/10.1175/BAMS-D-13-00255.1>
- Kidd, B., & Katzfuss, M. (2022). Bayesian nonstationary and nonparametric covariance estimation for large spatial data (with discussion). *Bayesian Analysis*, 17(1), 291–351. <https://doi.org/10.1214/21-BA1273>
- Klein, N., Hothorn, T., Barbanti, L., & Kneib, T. (2022). Multivariate conditional transformation models. *Scandinavian Journal of Statistics*, 49(1), 116–142. <https://doi.org/10.1111/sjos.12501>
- Kobyzev, I., Prince, S. J., & Brubaker, M. A. (2021). Normalizing flows: An introduction and review of current methods. *IEEE Transactions on Pattern Analysis and Machine Intelligence*, 43(11), 3964–3979. <https://doi.org/10.1109/TPAMI.2020.2992934>
- Krupskii, P., Huser, R., & Genton, M. G. (2018). Factor copula models for replicated spatial data. *Journal of the American Statistical Association*, 113(521), 467–479. <https://doi.org/10.1080/01621459.2016.1261712>
- Lang, S., & Brezger, A. (2004). Bayesian P-splines. *Journal of Computational and Graphical Statistics*, 13(1), 183–212. <https://doi.org/10.1198/1061860043010>
- Li, B., & Shand, L. (2022). Discussion of: "Bayesian nonstationary and nonparametric covariance estimation for large spatial data". *Bayesian Analysis*, 17(1), 291–351. <https://doi.org/10.1214/21-BA1273>
- Mondal, S., Krupskii, P., & Genton, M. G. (2024). A non-stationary factor copula model for non-Gaussian spatial data. *Stat*, 13(3), e715. <https://doi.org/10.1002/sta4.715>
- Müller, D., & Czado, C. (2019a). Selection of sparse vine copulas in high dimensions with the Lasso. *Statistics and Computing*, 29(2), 269–287. <https://doi.org/10.1007/s11222-018-9807-5>
- Müller, D., & Czado, C. (2019b). Dependence modelling in ultra high dimensions with vine copulas and the Graphical Lasso. *Computational Statistics & Data Analysis*, 137, 211–232. <https://doi.org/10.1016/j.csda.2019.02.007>
- Ng, T. L. J., & Zammit-Mangion, A. (2022). Spherical Poisson point process intensity function modeling and estimation with measure transport. *Spatial Statistics*, 50, 100629. <https://doi.org/10.1016/j.spasta.2022.100629>
- Ng, T. L. J., & Zammit-Mangion, A. (2023). *Mixture modeling with normalizing flows for spherical density estimation*. arXiv: 2301.06404 [stat]. <https://doi.org/10.48550/arXiv.2301.06404>
- Nychka, D., Hammerling, D., Krock, M., & Wiens, A. (2018). Modeling and emulation of nonstationary Gaussian fields. *Spatial Statistics*, 28, 21–38. <https://doi.org/10.1016/j.spasta.2018.08.006>

- Porcu, E., Bissiri, P. G., Tagle, F., Soza, R., & Quintana, F. A. (2021). Nonparametric Bayesian modeling and estimation of spatial correlation functions for global data. *Bayesian Analysis*, 16(3), 845–873. <https://doi.org/10.1214/20-BA1228>
- Pyä, N., & Wood, S. N. (2015). Shape constrained additive models. *Statistics and Computing*, 25(3), 543–559. <https://doi.org/10.1007/s11222-013-9448-7>
- Rasmussen, C. E., & Williams, C. K. I. (2008). *Gaussian processes for machine learning* (3. print). MIT Press.
- Riebl, H., Wiemann, P. F. V., & Kneib, T. (2023). *Liesel: A probabilistic programming framework for developing semi-parametric regression models and custom Bayesian inference algorithms*. arXiv: 2209.10975 [stat]. Retrieved January 29, 2024, from <http://arxiv.org/abs/2209.10975>
- Rigby, R. A., & Stasinopoulos, D. M. (2005). Generalized additive models for location, scale and shape. *Journal of the Royal Statistical Society: Series C (Applied Statistics)*, 54(3), 507–554. <https://doi.org/10.1111/j.1467-9876.2005.00510.x>
- Rigby, R. A., Stasinopoulos, M. D., Heller, G. Z., & De Bastiani, F. (2020). *Distributions for modeling location, scale, and shape*. Taylor & Francis.
- Risser, M. D. (2016). *Review: Nonstationary spatial modeling, with emphasis on process convolution and covariate-driven approaches*. arXiv: 1610.02447 [stat]. <https://doi.org/10.48550/arXiv.1610.02447>
- Rosenblatt, M. (1952). Remarks on a Multivariate Transformation. *The Annals of Mathematical Statistics*, 23(3), 470–472. <https://doi.org/10.1214/aoms/1177729394>
- Schäfer, F., Sullivan, T. J., & Owhadi, H. (2021). Compression, inversion, and approximate PCA of dense kernel matrices at near-linear computational complexity. *Multiscale Modeling & Simulation*, 19(2), 688–730. <https://doi.org/10.1137/19M129526X>
- Sklar, M. (1959). Fonctions de répartition à N dimensions et leurs marges. *Annales de l'ISUP*, 8(3), 229–231.
- van der Wilk, M., Dutordoir, V., John, S. T., Artemev, A., Adam, V., & Hensman, J. (2020). *A framework for interdomain and multioutput Gaussian processes*. arXiv: 2003.01115 [cs, stat]. Retrieved May 6, 2024, from <http://arxiv.org/abs/2003.01115>
- Wiens, A., Nychka, D., & Kleiber, W. (2020). Modeling spatial data using local likelihood estimation and a Matérn to spatial autoregressive translation. *Environmetrics*, 31(6), e2652. <https://doi.org/10.1002/env.2652>
- Xu, G., & Genton, M. G. (2017). Tukey g-and-h random fields. *Journal of the American Statistical Association*, 112(519), 1236–1249. <https://doi.org/10.1080/01621459.2016.1205501>